Chemical Science

ROYAL SOCIETY OF CHEMISTRY

EDGE ARTICLE

View Article Online
View Journal | View Issue

Check for updates

Cite this: *Chem. Sci.*, 2022, **13**, 8095

All publication charges for this article have been paid for by the Royal Society of Chemistry

# Pyridine dicarbanion-bonded $Ag_{13}$ organometallic nanoclusters: synthesis and on-surface oxidative coupling reaction†

Cui-Cui Li, Siqi Zhang, Jian Tang, Ruijun Jian, Yu Xia and Liang Zhao *

Received 16th February 2022
Accepted 13th June 2022

DOI: 10.1039/d2sc00989g

rsc.li/chemical-science

Highly reactive organometallic nanoclusters *in situ* generated in metal-catalyzed reactions are pivotal in the comprehension of catalytic mechanisms. Herein, we develop a two-step synthetic method to achieve three unprecedented aryl dicarbanion-bonded $Ag_{13}$ nanoclusters by using protective macrocyclic ligands. Firstly, various aryl dicarbanion–$Ag_4$ cluster intermediates are acquired *via* a silver-mediated annulation reaction within a macrocyclic ligand. These $Ag_4$ cluster precursors are released from the surrounding macrocycle by protonation, and further undergo an inter-cluster coupling to generate bipyridine products and low-valence silver atoms. The remaining resurgent diide–$Ag_4$ clusters assemble with low-valence silver atoms to yield a series of organometallic $Ag_{13}$ nanoclusters. These $Ag_{13}$ nanoclusters feature a unique open-shell electronic structure as well as a chiral cluster architecture due to the asymmetric arrangements of surrounding aryl dianion ligands. Furthermore, the pyridyl diide ligands on the surface of the nanocluster further experience an intra-cluster oxidative coupling to produce bipyridine coupling products and large nanoparticles. The coupling reaction-driven cluster-to-cluster transformation is comprehensively tracked by high resolution mass spectroscopy. This work is not only reminiscent of the detailed evolution of cluster species upon the occurrence of coupling reactions, but also reproduces novel inter- and intra-cluster coupling steps at different reaction stages.

## Introduction

The study of metal subnano- or nano-clusters *in situ* generated in transition metal-catalyzed reactions has become a fascinating and substantial topic in both homogeneous and heterogeneous catalyses.[1] These kinds of metal nanoclusters, which are mostly formed through the reduction of metal complexes by reaction substrates, coordinative ligands or additives,[1f,2] largely reshape the perception regarding real catalytic species and detailed catalytic mechanisms. They act as either catalytically active species[1d,f,3] or alternative reservoirs of active metal complexes,[4] and prevent devitalization of the catalytic species by suppressing the formation of insoluble metal species. Structural investigations on the *in situ* generated metal nanocluster intermediates, especially carbon-bonded organometallic nanoclusters, enable chemists to gain insight into the structural details of privileged intermediates and promote the comprehension of catalytic mechanisms. However, although organometallic clusters have been identified as intermediate species in many metal-catalyzed organic transformations by mass spectrometry,[3d,5] electron microscopy[2a,3a] and X-ray absorption spectroscopy,[3b,c] their synthesis and structural characterization are still a challenging task due to their transient and highly reactive nature. Accordingly, the transformations of organic ligands attaching on these organometallic nanoclusters are rarely investigated.[6]

The Ag(0/I)-based single-electron redox cycle has been extensively proposed in many silver-catalyzed coupling reactions.[7] The presence of low valence silver atoms in the Ag(0/I) redox process facilitates the *in situ* formation of silver nanoclusters, which have been demonstrated to exhibit excellent catalytic activity in organic transformations.[8] However, in-depth structural characterization and reactivity studies of these *in situ* generated silver nanoclusters suffer from the lack of appropriate synthetic methods and stabilizing means as labile silver–carbon bonds prefer a rapid homolysis disproportionation to generate metallic silver and finally cause decomposition.[9] In view of the previously reported successful encapsulation and stabilization of reactive organometallic species within supramolecular cages,[10] we envision that the initial encaging of organosilver species within a closed macrocyclic environment followed by a steerable organometallic transformation may provide a viable pathway to acquire organosilver nanoclusters (Scheme 1).

*Key Laboratory of Bioorganic Phosphorus Chemistry & Chemical Biology, Department of Chemistry, Tsinghua University, Beijing 100084, China. E-mail: zhaolchem@mail.tsinghua.edu.cn*

† Electronic supplementary information (ESI) available. CCDC 1995296, 1995303, 1996369, 2060712, 2062348, 2062349, 2062351, 2062353 and 2175048. For ESI and crystallographic data in CIF or other electronic format see https://doi.org/10.1039/d2sc00989g

Open Access Article. Published on 14 June 2022. Downloaded on 1/1/2026 2:59:02 AM.
This article is licensed under a Creative Commons Attribution-NonCommercial 3.0 Unported Licence.

Open Access Article. Published on 14 June 2022. Downloaded on 1/1/2026 2:59:02 AM.
This article is licensed under a Creative Commons Attribution-NonCommercial 3.0 Unported Licence.

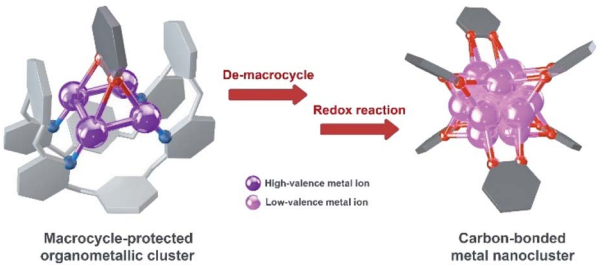


Scheme 1 Synthesis of carbon-bonded metal nanoclusters *via* the transformation of macrocycle-protected organometallic clusters.

In this work, we develop a two-step synthetic method to achieve a series of unprecedented aryl vicinal dicarbanion bonded $Ag_{13}$ nanoclusters ($[Ag_{13}(^{R}Py–H)_6](CF_3SO_3)_6$, R = Me, *n*-Pr, Ph). At the initial step, differently substituted pyridine dicarbanion-bonded $Ag_4$ cluster intermediates are acquired *via* a silver-mediated cyclization reaction within a macrocyclic ligand. After removing the protective macrocycle by protonation, the dicarbanion–$Ag_4$ cluster precursors undergo an inter-cluster oxidative coupling between two pyridine carbanions to *in situ* generate low-valence silver atoms. The remaining released dicarbanion–$Ag_4$ clusters assemble with a low-valence silver atom to yield vicinal dicarbanion bonded $Ag_{13}$ nanoclusters. These organometallic nanoclusters feature a unique open-shell electronic structure as well as a chiral cluster architecture as a result of asymmetric arrangement of surrounding pyridyl dianion ligands. Furthermore, the pyridyl dicarbanion ligands on the surface of a $Ag_{13}$ nanocluster can undergo an intra-cluster oxidative coupling to generate the bipyridine coupling product and large nanoparticle species, reminiscent of the evolution of cluster species in many metal-catalyzed reactions. This work not only reveals novel dicarbanion-bonded metal nanoclusters for the first time, but also provides a new perspective for the dynamic evolution of organometallic species in metal catalysis, from isolated single atom species through low-nuclear clusters to nanoclusters along with the occurrence of intra- and inter-cluster coupling reactions.

## Results and discussion

### Pyridyl dicarbanion bonded $Ag_{13}$ nanoclusters

In this work, an attempt was made to generate a *gem*-dimetallic organometallic species as a representative intermediate motif in metal-catalyzed reactions.[11] To achieve this goal, a silver(I)-mediated intermolecular annulation reaction of ketones and propargylamine[12] was performed in the presence of excessive silver salts and a polydentate macrocyclic ligand octamethylazacalix[8]pyridine (**Py[8]**).[13] As shown in Fig. 1, various methyl ketones together with propargylamine undergo a continuous multi-step transformation of condensation, imine–enamine isomerization, 6-*endo-dig* cyclization and oxidative aromatization to yield three differently substituted pyridyl dicarbanion bonded $Ag_4$ clusters (abbreviated as $^{Me}$**PyAg$_5$**, $^{n\text{-}Pr}$**PyAg$_5$** and $^{Ph}$**PyAg$_5$**) in moderate yields (23–61%). The composition and structural features of these $Ag_4$ clusters were confirmed by high-resolution electrospray ionization mass spectrometry (Fig. S1–S3†) and NMR (Fig. S4–S7†).

Crystalline solids of these organosilver cluster compounds are quite stable in the dark even upon exposure to air and moisture for months. The $^1$H NMR monitoring on the acetone solution of $^{Me}$**PyAg$_5$** shows negligible change for up to seven days (Fig. S8†), suggesting its superior stability in the solution state. Single-crystal X-ray analysis reveals a highly isostructural pyridyl diide–$Ag_4$ cluster core in $^{Me}$**PyAg$_5$** (Fig. 1), $^{n\text{-}Pr}$**PyAg$_5$**

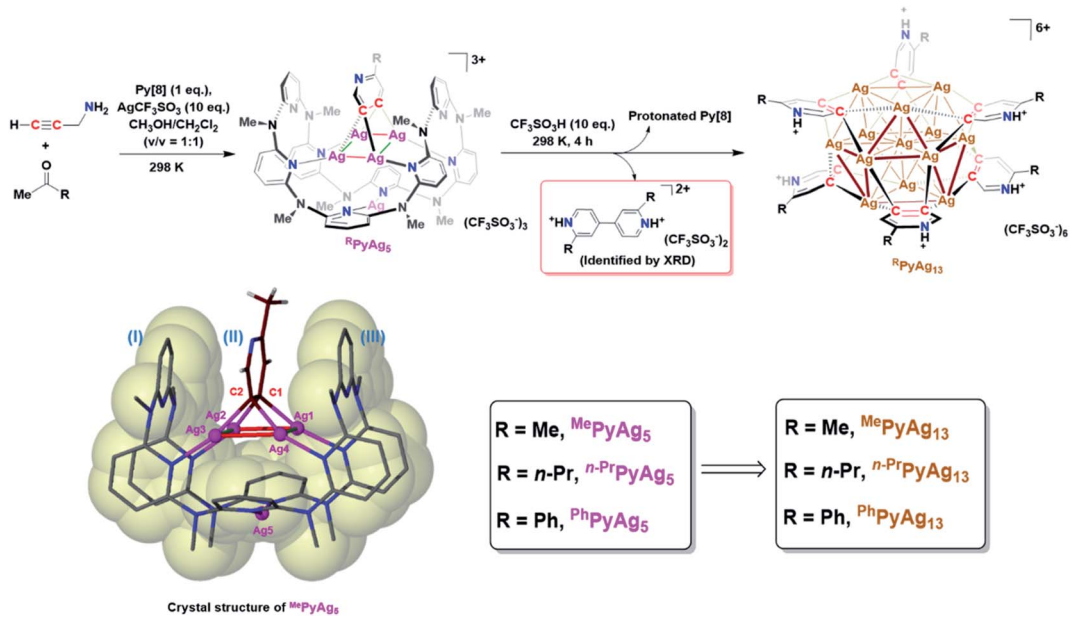


Fig. 1 Synthetic procedures for macrocycle-protected $Ag_4$ cluster complexes and aryl vicinal dicarbanion bonded $Ag_{13}$ nanoclusters. The crystal structure of $^{Me}$**PyAg$_5$** is shown as an inset with anions and solvent molecules omitted for clarity.


© 2022 The Author(s). Published by the Royal Society of Chemistry

Open Access Article. Published on 14 June 2022. Downloaded on 1/1/2026 2:59:02 AM. This article is licensed under a Creative Commons Attribution-NonCommercial 3.0 Unported Licence.

(Fig. S9†) and $^{Ph}$**PyAg$_5$** (Fig. S10†). Taking $^{Me}$**PyAg$_5$** for instance, two vicinal carbon atoms C1 and C2 of a pyridyl ring are negatively charged and stabilized by a coplanar argentophilic $Ag_4$ rectangle *via* four-fold Ag–C σ bonds in the range of 2.148(9)–2.181(9) Å, which are comparable to the $CAg_2$ species in reported arylsilver(I) complexes.[10e,14] The $Ag_4$ rectangle is composed of two short Ag–Ag edges (Ag1–Ag2: 2.724(1) Å, Ag3–Ag4: 2.683(1) Å) and two long ones (Ag1–Ag4: 3.164(1) Å, Ag2–Ag3: 3.246(2) Å). The whole pyridyl diide–$Ag_4$ cluster motif is enclosed by a semi-open bowl-shaped macrocyclic ligand **Py[8]** *via* four-fold Ag–N bonds. Another silver atom is clamped by two pyridyl nitrogen atoms at the bottom of the bowl. It should be emphasized that the metalated pyridyl diide is sandwiched by two parallel pyridyl rings of **Py[8]**, leading to a fully eclipsed face-to-face π–π stacking with small dihedral angles ($\theta_{I-II} = 5.0°$ and $\theta_{II-III} = 4.4°$) and displacement distances ($D_{I-II} = 0.738$ Å and $D_{II-III} = 0.523$ Å). This unusual eclipsed face-to-face π–π stacking is in sharp contrast to the common displaced π–π stacking between aromatic rings as a result of the requirement of mitigated π–π electron repulsion.[15] Theoretical studies reveal that the $p_\pi$ electrons of the central metalated pyridine largely participate in the C–$Ag_2$ multi-centered bonding (Fig. S11†) and thus weaken the π–π repulsion with two bilateral pyridine rings belonging to the peripheral **Py[8]**.

With the macrocycle-protected organosilver cluster intermediates in hand, we subsequently removed the protective **Py[8]** by protonation to initiate transformations of the diide–$Ag_4$ clusters. After screening several acids with a wide range of p$K_a$ values (Fig. S12†), the strong trifluoromethanesulfonic acid $CF_3SO_3H$ was selected because of the prompt generation of protonated **Py[8]** as a white precipitate (Fig. S13†) upon the addition of $CF_3SO_3H$ to the acetone solution of $^{Me}$**PyAg$_5$**. This protonation process was simultaneously accompanied by a gradual solution color change from light yellow to brown. Diffusion of diethyl ether into the brown solution deposited two types of brown and colorless crystals in a yield of 52% (Table S1†) and 13%, respectively.

X-ray crystallographic analysis of the $^{Me}$**PyAg$_5$**-derived brown crystalline sample reveals that its structure includes a twisted cuboctahedral $Ag_{13}$ core, which is peripherally wrapped by six 2-methylpyridyl diides *via* a $\mu_4$-C,C-$\eta^2$,$\eta^2$ mode and five coordinative triflate anions (Fig. 2a). There is one free $CF_3SO_3^-$ serving as an uncoordinated counter anion. This $Ag_{13}$ nanocluster is different from the reported $Ag_{13}$ cuboctahedron, each triangle face of which is capped by an $Fe(CO)_4$ group to generate a $[Ag_{13}Fe_8(CO)_{32}]^{4-}$ cluster.[16] The electrospray ionization mass spectroscopy (ESI-MS) study on the solution of the brown crystals gives rise to two isotopically well-resolved peaks at $m/z$ = 2847.7750 and 2865.7704, which can be assigned to the species $\{[Ag_{13}(^{Me}Py–H)_6](CF_3SO_3)_6\}^+$ and $\{[Ag_{13}(^{Me}Py–H)_6](CF_3SO_3)_6 \cdot H_2O\}^+$, respectively (Fig. S14†). This result indicates that six 2-methylpyridyl diides around the cluster core are all protonated at the pyridyl nitrogen atoms. In the light of the charge balance requirement, we assume that the 13-membered silver cluster core shows twelve positive charges and has an unpaired electron, which is similar to the paramagnetic $[Ag_{13}Fe_8(CO)_{32}]^{4-}$ cluster.[16] This conjecture is supported by electron paramagnetic resonance (EPR) measurement (Fig. S15†)[16] and X-ray photoelectron spectroscopy (XPS, (Fig. S16†)). The XPS spectra revealed two intensive peaks in the Ag 3d region at 374.9 and 368.9 eV corresponding to Ag $3d_{3/2}$ and Ag $3d_{5/2}$, respectively (Fig. S16b†). The peak could be deconvoluted into 375.5 eV ($3d_{3/2}$, $Ag^0$), 374.9 eV ($3d_{3/2}$, $Ag^+$), 369.5 eV ($3d_{5/2}$, $Ag^0$) and 368.9 eV ($3d_{5/2}$, $Ag^+$). The area ratios of $Ag^+/Ag^0$ for Ag $3d_{3/2}$ and Ag $3d_{5/2}$ are 11 : 1 and 10 : 1, basically consistent with the presence of two kinds of $Ag^+$ and $Ag^0$ in the crystal structure. Based on the Auger electron spectroscopy (AES) data under X-ray irradiation of 1486.6 eV, the Auger parameters of $Ag^+$ and $Ag^0$ are deduced to be 724.5 and 725.1 eV, which are in good agreement with those of $Ag_2O$ (Auger parameter: 724.5 eV)[17] and Ag(0) (Auger parameter: 726.0 eV).[18] Consequently, the molecular formula of the brown crystals is determined to be $[Ag_{13}(^{Me}Py–H)_6](CF_3SO_3)_6$ ($^{Me}$**PyAg$_{13}$**). The existence of low valence silver atoms in the $[Ag_{13}]^{12+}$ core of $^{Me}$**PyAg$_{13}$** implies that some Ag(I) ions were reduced during the construction of $^{Me}$**PyAg$_{13}$**, which is supported by further X-ray crystallographic analysis of the colorless crystals (Fig. 1). The identification of the colorless crystalline product as protonated 2,2′-dimethyl-4,4′-bipyridine (Fig. S17 and S18†) clearly indicates the occurrence of a two-electron oxidative coupling between two $C_1$–$Ag_2$ units from two individual 2-methylpyridine–$Ag_4$ motifs. This coupling process simultaneously generates low valence silver atoms. In view of the high similarity of pyridyl $C_2$–$Ag_4$ moieties between $^{Me}$**PyAg$_5$** and $^{Me}$**PyAg$_{13}$**, we deduce that the 13-membered nanocluster core in $^{Me}$**PyAg$_{13}$** arises from the assembly of low valence silver atoms with remaining protonated 2-methylpyridine diide–$Ag_4$ motifs *in situ* released from the **Py[8]** macrocycle of $^{Me}$**PyAg$_5$** (Fig. 1 and S19†).

The twisted cuboctahedral $Ag_{13}$ core in $^{Me}$**PyAg$_{13}$** is divided into three layers of $Ag_3$–$Ag_7$–$Ag_3$, and the distances between the central silver (Ag1) and the upper and lower $Ag_3$ layers are 2.331 and 2.328 Å, respectively (Fig. 2b). The argentophilic distances between the central silver atom Ag1 and twelve surface silver ions are in the range of 2.863(2)–3.167(2) Å (yellow color in Fig. 2b), which are comparable with the Ag–Ag distances in $[Ag_{13}Fe_8(CO)_{32}]^{4-}$ (2.923 Å). The other 24 surficial argentophilic edges among twelve peripheral silver atoms can be classified into two types. The short edges bridged by the same diide carbon atom (average distances: 2.755 Å, red color in Fig. 2b) and the long ones spanned by two diide carbon atoms of the same pyridine ring (average distances: 3.205 Å, green color in Fig. 2b) are comparable to those in the parent tetranuclear cluster $^{Me}$**PyAg$_5$** (2.703 Å and 3.192 Å, respectively). The maximum value of the argentophilic distance alternations between the long and short edges in $^{Me}$**PyAg$_{13}$** is 0.621 Å, which is significantly larger than that in $[Ag_{13}Fe_8(CO)_{32}]^{4-}$.[16] In addition, six protonated 2-methylpyridine diide ligands each is enveloped by a rectangular plane of the $Ag_{13}$ core through four-fold Ag–C bonds in the range of 2.12(2)–2.29(3) Å, which are slightly longer than the Ag–C bonds in $^{Me}$**PyAg$_5$**. Notably, the protonated 2-methylpyridine diide ligands on both upper (I, II and III) and lower layers (IV, V and VI) exhibit different orientations (Fig. 2a). Therein, four diide ligands (I, III, IV and V in pink color) are equatorially bonded to the $Ag_{13}$ core, while the

Open Access Article. Published on 14 June 2022. Downloaded on 1/1/2026 2:59:02 AM.
This article is licensed under a Creative Commons Attribution-NonCommercial 3.0 Unported Licence.

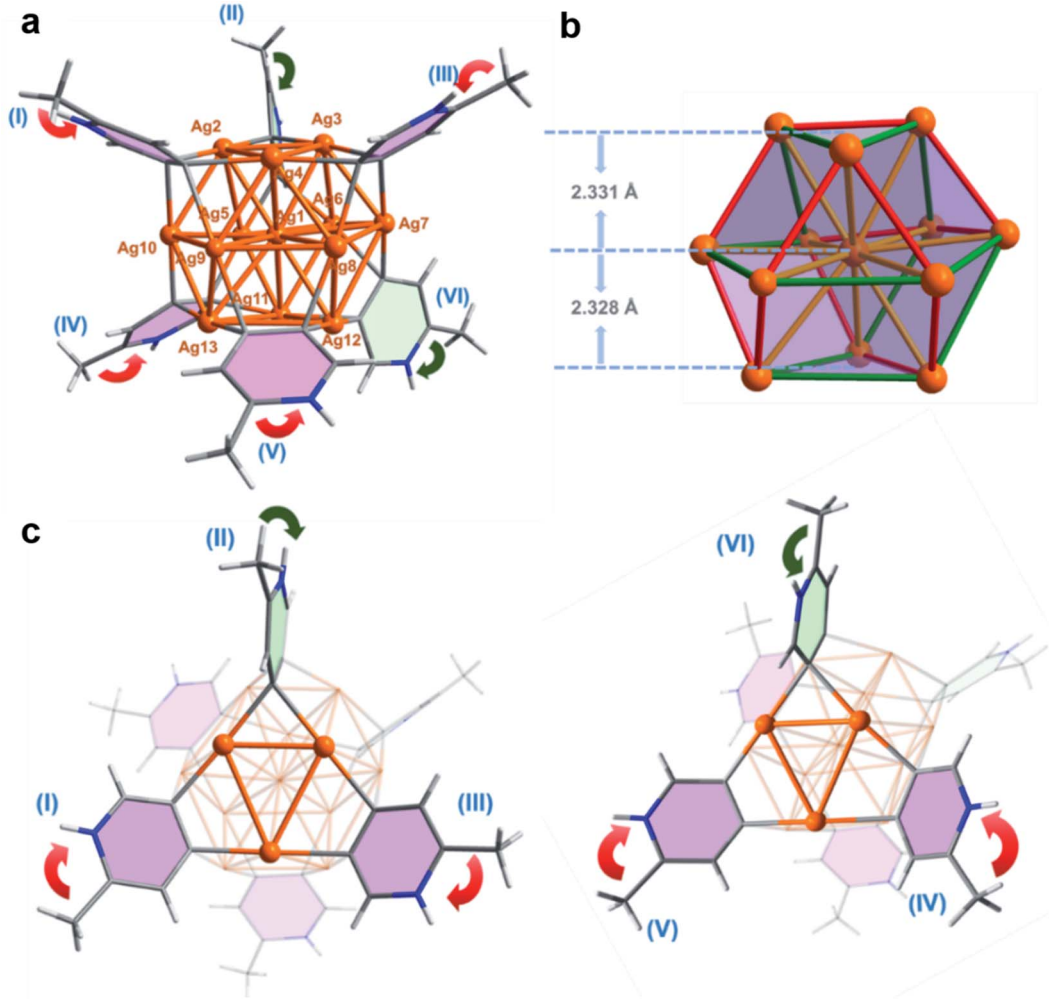


Fig. 2 (a) Crystal structure of $^{Me}PyAg_{13}$ containing equatorial (pink) and axial (light green) 2-methylpyridyl diide ligands. Peripheral $CF_3SO_3^-$ anions are omitted for clarity. (b) The $Ag_{13}$ kernel in $^{Me}PyAg_{13}$. Color coding: Ag, brown; C, gray; H, white; N, blue. (c) Arrangement of the orientated 2-methylpyridine rings attached on the $Ag_{13}$ kernel at the upper and nether sides in $^{Me}PyAg_{13}$. Selected bond lengths (Å) of $^{Me}PyAg_{13}$ highlighted in yellow: Ag1–Ag2 2.885(2); Ag1–Ag3 2.897(2); Ag1–Ag4 3.025(2); Ag1–Ag5 2.947(2); Ag1–Ag6 3.167(2); Ag1–Ag7 2.986(2); Ag1–Ag8 2.930(2); Ag1–Ag9 3.062(2); Ag1–Ag10 2.915(2); Ag1–Ag11 2.929(2); Ag1–Ag12 2.863(2); Ag1–Ag13 3.038(2); red: Ag2–Ag3 2.780(2); Ag2–Ag10 2.825(3); Ag4–Ag9 2.716(3); Ag4–Ag8 2.758(2); Ag3–Ag7 2.763(2); Ag5–Ag6 2.718(2); Ag5–Ag11 2.736(2); Ag10–Ag13 2.716(2); Ag9–Ag13 2.737(3); Ag8–Ag12 2.817(2); Ag6–Ag7 2.701(2); Ag11–Ag12 2.796(2); green: Ag2–Ag4 3.218(2); Ag3–Ag4 3.256(2); Ag10–Ag9 3.089(2); Ag8–Ag7 3.253(2); Ag2–Ag5 3.281(2); Ag3–Ag6 3.078(2); Ag5–Ag10 3.223(2); Ag11–Ag13 3.024(2); Ag8–Ag9 3.022(2); Ag12–Ag13 3.322(2); Ag7–Ag12 3.196(2); Ag6–Ag11 3.164(2).

other two (II and VI in light green color) are in an axial orientation. The biased spatial arrangement of the protonated 2-methylpyridine ligands can be described by the arrow vector from the methyl substituent toward the pyridyl nitrogen. As to the four equatorial 2-methylpyridine ligands, I and III on the upper layer are related by a $C_3$-axis, while IV and V on the nether layer have a mirror symmetry (red arrows in Fig. 2c). On the other hand, the axial 2-methylpyridine ligand II is in an *endo*-form with the methyl group close to the silver nanocluster, while ligand VI shows an *exo*-form with the methyl group pointing away from the cluster core (green arrows in Fig. 2c). In this way, the twelve peripheral silver ions (from Ag2 to Ag13) of the $Ag_{13}$ core are coordinated by two kinds of pyridyl carbon atoms ($C_{para}$ and $C_{meta}$ refer to the 4- and 5-position carbon atom on the pyridine ring, respectively) in three combinations of $C_{para}$–Ag–$C_{para}$, $C_{para}$–Ag–$C_{meta}$ and $C_{meta}$–Ag–$C_{meta}$ (Fig. S20†). The differentiated orientation of the total six 2-methylpyridyl diide ligands breaks the symmetry and thus imparts chirality to the whole cluster structure of $^{Me}PyAg_{13}$, making it the first $\{M_{13}\}$-type chiral metal nanocluster to our knowledge.[19] Herein, both cluster enantiomers are present in the crystal structure of $^{Me}PyAg_{13}$ (Fig. S21†).

We next carried out density functional theory (DFT) calculations to investigate the bonding and argentophilic interaction in $^{Me}PyAg_{13}$. The Wiberg bond order[20] based on the Löwdin orthogonalized basis was calculated and summarized in Table S2.† The sum of Ag–C bond orders for each $CAg_2$ species is close to one (0.893–0.975) and the multi-center bond order (MCBO, Table S3†) of each $CAg_2$ species ranges from 0.013 to 0.091, suggesting the formation of a 3c–2e bonding in each $CAg_2$


© 2022 The Author(s). Published by the Royal Society of Chemistry

Open Access Article. Published on 14 June 2022. Downloaded on 1/1/2026 2:59:02 AM. This article is licensed under a Creative Commons Attribution-NonCommercial 3.0 Unported Licence.

species. In addition, the Ag–Ag Wiberg bond order of $^{Me}$**PyAg$_{13}$** is in the range of 0.189–0.384 as a result of significant argentophilic interaction between two silver atoms. Therein, the average Wiberg bond order of short Ag–Ag edges (red color in Fig. 2b) in a cuboctahedral $Ag_{13}$ core is 0.359, while those of the long Ag–Ag edges (green color in Fig. 2b) and twelve central ones (yellow color in Fig. 2b) are 0.222 and 0.260, respectively. The independent gradient model based on Hirshfeld partition (IGMH)[21] was further carried out *via* sign($\lambda_2$)$\rho$ functions to examine intramolecular interactions in $^{Me}$**PyAg$_{13}$**. From the IGMH map, the mazarine area between six 2-methylpyridyl diides and the $Ag_{13}$ core (Fig. S22a†) indicates prominent electron density in these regions and covalent characteristics of the C–Ag bonds. Furthermore, there are blue areas in the isosurface between two adjacent silver atoms, suggesting the presence of apparent argentophilic interaction within the $Ag_{13}$ core (Fig. S22b and c†).

The Atoms in Molecules (AIM) analysis[22] also confirms strong argentophilic interaction in $^{Me}$**PyAg$_{13}$**. As shown in Fig. S23,† the bond critical points exist in each pair of adjacent silver atoms. The negative bond degree parameter (BD = $E(r)/\rho(r)$, $E(r)$ and $\rho(r)$ being the total electron energy density and the electron density value at the Ag–Ag (3, −1) critical point) and the ratio $|V(r)|/G(r) > 1$ ($V(r)$ and $G(r)$ being the pressures exerted on and by the electrons at the Ag–Ag (3, −1) critical point),[23] indicate apparent argentophilic interactions in the $Ag_{13}$ core (Table S4†). It is worth noting that some bond critical points lie between H atoms of 2-methylpyridyl diides and F or O atoms of $CF_3SO_3^-$, suggesting that multiple hydrogen bonding is instrumental in the stabilization of $^{Me}$**PyAg$_{13}$**.

Our two-step synthetic strategy is also applicable in the synthesis of $^{n\text{-}Pr}$**PyAg$_{13}$** and $^{Ph}$**PyAg$_{13}$** by the reaction of differently substituted $^{n\text{-}Pr}$**PyAg$_5$** or $^{Ph}$**PyAg$_5$** with $CF_3SO_3H$, respectively. Similarly, during the acidification of $^{n\text{-}Pr}$**PyAg$_5$** or $^{Ph}$**PyAg$_5$**, the coupling product 2,2′-dipropyl-4,4′-bipyridine or 2,2′-diphenyl-4,4′-bipyridine was detected and successfully characterized by mass spectrometry (Fig. S24 and S25†) and single crystal XRD analysis (Fig. S26 and S27†). XRD crystallographic analysis, high-resolution ESI-MS and UV-vis absorption spectra reveal that $^{n\text{-}Pr}$**PyAg$_{13}$** (Fig. 3a, S28 and S29†) and $^{Ph}$**PyAg$_{13}$** (Fig. 3b and S30–S32†) are isostructural with $^{Me}$**PyAg$_{13}$** in the aspects of bond distances and angles. Nevertheless, the dihedral angles between the upper and lower $Ag_3$ planes in $^{n\text{-}Pr}$**PyAg$_{13}$** and $^{Ph}$**PyAg$_{13}$** are 11.5° and 11.7°, respectively (Table S5†), a bit higher than that of $^{Me}$**PyAg$_{13}$** (9.7°). In addition, the mean deviation of the central $Ag_7$ layer in $^{n\text{-}Pr}$**PyAg$_{13}$** and $^{Ph}$**PyAg$_{13}$** is 0.125 and 0.104 Å, respectively, also larger than that of $^{Me}$**PyAg$_{13}$** (0.094 Å). The more distorted $Ag_{13}$ core in $^{n\text{-}Pr}$**PyAg$_{13}$** and $^{Ph}$**PyAg$_{13}$** should be ascribed to significant steric hindrance among peripheral *n*-propyl and phenyl substituents. Furthermore, in contrast to the *exo* and *endo* spatial orientations of two axial pyridyl diide ligands in $^{n\text{-}Pr}$**PyAg$_{13}$** and $^{Me}$**PyAg$_{13}$**, $^{Ph}$**PyAg$_{13}$** has two axial 2-phenylpyridine ligands II and VI both in the *exo*-form with the phenyl group pointing away from the cluster core (green arrows in Fig. 3b). This structural difference underlines the oriented diversity of the pyridyl diide ligands around the $Ag_{13}$ nanocluster core.

The newly synthesized $Ag_{13}$ nanoclusters retain their structures intact in solution based on the $^1$H-NMR and ESI-MS spectra. In the $^1$H NMR spectrum of $^{Me}$**PyAg$_{13}$**, three sets of aromatic resonance peaks at 8.94, 8.31–8.19 and 7.98 ppm with a ratio of 1 : 10 : 1 were observed (Fig. S33†). This unusual integral ratio corresponding to the pyridyl protons in $^{Me}$**PyAg$_{13}$** may be due to different configurational isomers in solution or differentiated ligand orientations in $^{Me}$**PyAg$_{13}$**. Diffusion ordered spectroscopy (DOSY) of $^{Me}$**PyAg$_{13}$** (Fig. S34†) shows only one diffusion coefficient of $D = 7.35 \times 10^{-10}$ m$^2$ s$^{-1}$ for the pyridyl proton peaks (Table S6†). Based on the Stokes–Einstein equation, the calculated diameter was 18.75 Å, which agrees well with the measured distances in the crystal structure of

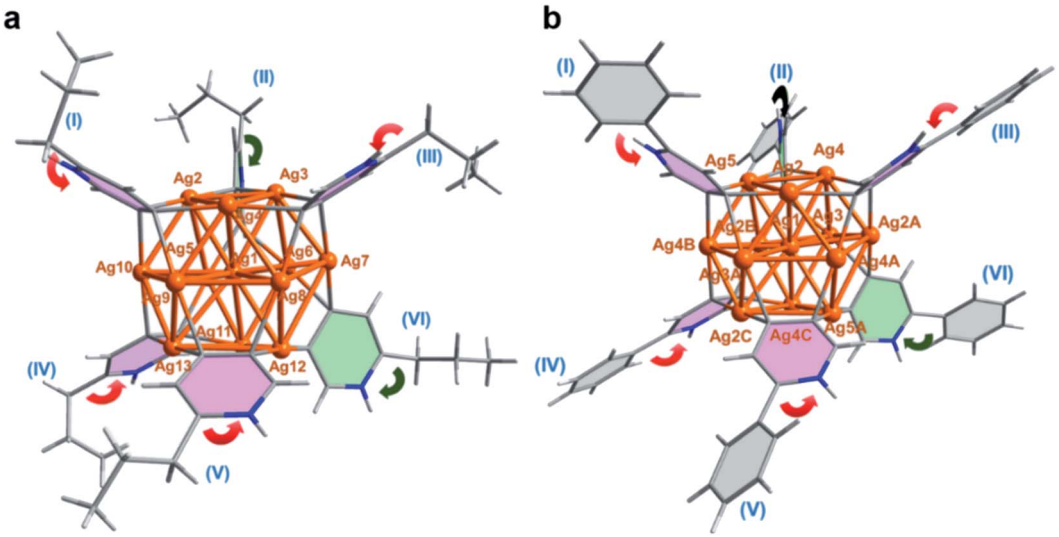


Fig. 3 Crystal structures of the $Ag_{13}$ nanoclusters in (a) $^{n\text{-}Pr}$**PyAg$_{13}$** and (b) $^{Ph}$**PyAg$_{13}$** with equatorial (pink) and axial (light green) pyridyl ligands. Peripheral $CF_3SO_3^-$ anions and solvent molecules are omitted for clarity. Color coding: Ag, brown; C, gray and blue gray; H, white; N, blue.

Open Access Article. Published on 14 June 2022. Downloaded on 1/1/2026 2:59:02 AM.
This article is licensed under a Creative Commons Attribution-NonCommercial 3.0 Unported Licence.

$^{Me}PyAg_{13}$ (17.55 Å). Besides, variable temperature $^1$H NMR spectra (Fig. S35†) and UV-vis spectra (Fig. S36†) display negligible changes with the temperature increase from 298 to 353 K, excluding the possibility of other equilibrium cluster conformations in solution. Therefore, the aromatic integral ratio of 1 : 10 : 1 may correspond to 12 inequitable pyridyl protons of six diide ligands. In order to accurately assign the twelve pyridyl proton atoms, the NMR spectrum of $^{Me}PyAg_{13}$ was simulated by the scaling method based on an optimized structure. The simulated results show that the proton signal at 8.94 ppm corresponds to the proton atom attaching on the carbon atom C6 (adjacent to the pyridyl nitrogen) in ligand VI, and the peak at 7.98 ppm is assigned to the C3 hydrogen atom (*meta*-position to the pyridyl nitrogen) of II (Fig. S37a†). In addition, the chemical shifts of the remaining ten protons are also inequivalent but very close, which are finely influenced by the ligand orientation and the C–$Ag_2$ units (Fig. S37b†). The $^1$H NMR spectrum of $^{n\text{-}Pr}PyAg_{13}$ (Fig. S38†) is very similar to that of $^{Me}PyAg_{13}$ because of their completely consistent ligand orientation scenario. In contrast, the $^1$H NMR spectrum of $^{Ph}PyAg_{13}$ shows four broad resonance peaks at 8.77, 8.53, 7.90 and 7.66 ppm with an integral ratio of 6 : 6 : 12 : 18 (Fig. S39†). The simulated $^1$H NMR spectrum of $^{Ph}PyAg_{13}$ (Fig. S40a†) indicates that the resonances at 8.77 and 8.53 ppm are assigned to the protons on the *meta* and *ortho* positions of the pyridine rings in $^{Ph}PyAg_{13}$, and the peaks at 7.90 and 7.66 ppm correspond to the protons on the phenyl rings (Fig. S40b†). The above experimental and theoretical NMR results suggest that distinct spatial arrangements of the pyridyl diide ligands lead to biased charge distribution on carbon atoms and thus account for inequivalent proton NMR peaks.

## Inter- and intra-cluster coupling of diide ligands

To gain further insight into the formation process of $Ag_{13}$ nanoclusters, we conducted a cross experiment between the same equivalent $^{Me}PyAg_5$ and $^{n\text{-}Pr}PyAg_5$ with $CF_3SO_3H$ in acetone. The ESI-MS monitoring showed a normal distribution of various $Ag_{13}$ nanoclusters containing a ligand combination of protonated $^{Me}Py$ and $^{n\text{-}Pr}Py$ in a ratio from 1 : 5 to 5 : 1 (Fig. 4a and Table S7†). In addition, the cross-coupling product 2-methyl-2′-propyl-4,4′-bipyridine was determined as the primary coupling species in ESI-MS spectra, wherein the minor homo-coupling products 2,2′-dimethyl-4,4′-bipyridine and 2,2′-dipropyl-4,4′-bipyridine were observed as well. This ESI-MS evidence suggests that the initial formation of the $Ag_{13}$ nanoclusters mostly relies on random combinations of two types of resurgent pyridyl diide–$Ag_4$ clusters as they are released from the protective macrocycles.

We next studied the transformation of diide ligands on the surface of $^{Me}PyAg_{13}$. The addition of $CF_3SO_3H$ to the methanol solution of $^{Me}PyAg_{13}$ also led to the coupling product 2,2′-dimethyl-4,4′-bipyridine in a high yield of 67%. In order to ensure the occurrence of intra-cluster coupling, the cross experiment by using equivalent $^{Me}PyAg_{13}$ and $^{n\text{-}Pr}PyAg_{13}$ was implemented. The homo-coupling compounds 2,2′-dimethyl-4,4′-bipyridine and 2,2′-dipropyl-4,4′-bipyridine were detected as major products in the ESI-MS monitoring (Fig. 4b), while only slight cross-coupling product 2-methyl-2′-propyl-4,4′-bipyridine was observed. In contrast to the prompt inter-cluster coupling among pyridyl diide–$Ag_4$ clusters at the initial stage, the coupling reaction of diide ligands around a single $Ag_{13}$ nanocluster at the second stage is relatively sluggish as indicated by

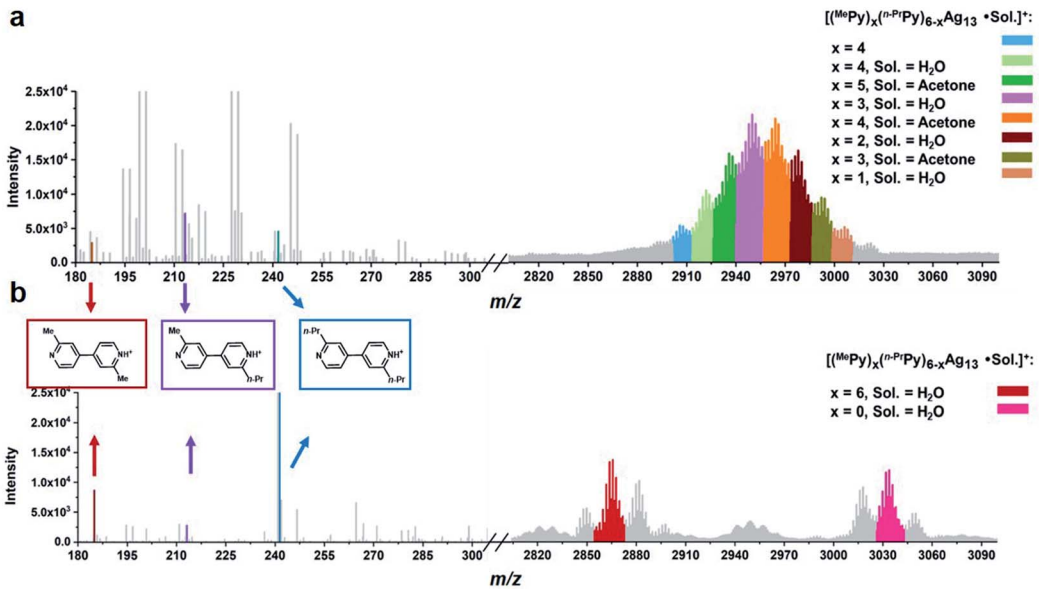


Fig. 4 ESI mass spectra of the acidifying solution samples containing equivalent (a) $^{Me}PyAg_5$ and $^{n\text{-}Pr}PyAg_5$ in acetone, and (b) $^{Me}PyAg_{13}$ and $^{n\text{-}Pr}PyAg_{13}$ in acetone.


© 2022 The Author(s). Published by the Royal Society of Chemistry

Open Access Article. Published on 14 June 2022. Downloaded on 1/1/2026 2:59:02 AM. This article is licensed under a Creative Commons Attribution-NonCommercial 3.0 Unported Licence.

the detection of unreactive $Ag_{13}$ clusters even after four days (Fig. S41†). Meanwhile, spherical nanoparticles with the sizes in the range of 20–40 nm were identified by transmission electron microscopy (TEM) images (Fig. S42†), suggesting the formation of larger nanocluster species by the association and merging of $Ag_{13}$ nanoclusters after the occurrence of intra-cluster oxidative coupling. Furthermore, infrared spectra of the solid originated from the $Ag_{13}$–$CF_3SO_3H$ mixture exhibit two stretching vibrations at 1540 $cm^{-1}$ and 1443 $cm^{-1}$ (Fig. S43†), which can be assigned to the characteristic absorption peaks of a pyridine ring. This result indicates that the larger Ag nanocluster species are still coordinated by pyridine ligands. Along with the prolongation of the reaction time, a black precipitate due to the further aggregation of large nanoparticles was observed.

Combining the above experimental results, we propose two phases of inter- and intra-cluster coupling accompanied by the structural evolution of silver cluster species from organic diide–$Ag_4$ clusters through $Ag_{13}$ nanoclusters to large nanoparticles. As shown in Fig. 5, the removal of protective **Py[8]** macrocycles by protonation makes the released organic diide–$Ag_4$ clusters randomly combine together and undergo a two-electron oxidative coupling to generate low valence silver atoms. The remaining protonated diide–$Ag_4$ clusters then assemble with the low valence silver atoms to produce the $Ag_{13}$ nanoclusters. In the second phase, the aryl dicarbanion ligands on the surface of a $Ag_{13}$ nanocluster experience protolysis at a [C–$Ag_2$] position and the remaining [C–$Ag_2$] site at the *para* position undergoes an intra-cluster oxidative coupling to generate homo-coupling bipyridine products and expedite the formation of large nanoparticle species. It is worth noting that the oxidative coupling of organic species around *in situ* generated metal subnano- or nano-clusters has been proposed in many metal-catalyzed reactions.[1a,h] However, there has been little knowledge about the rationality of such mechanism and structural details of related intermediates. The present transformation from isolated mononuclear metal complexes through low nuclearity clusters to nanoclusters and nanoparticles is reminiscent of the dynamic structural evolution of cluster species in those metal-catalyzed reactions, and also gives important insights into the coupling process of organic ligands at different reaction stages.

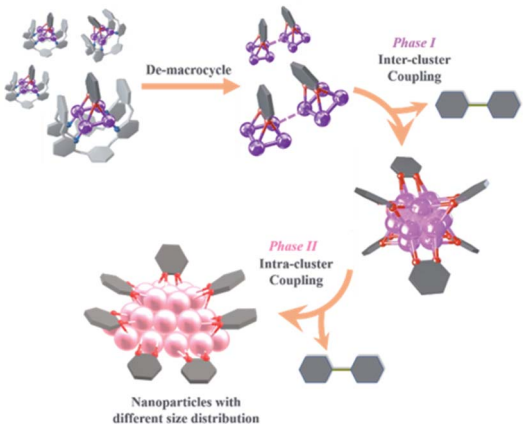


Fig. 5 Structural evolution of organosilver species from organic diide–$Ag_4$ clusters through nanoclusters to nanoparticles along with the occurrence of coupling reactions at different stages.

## Conclusion

In this work, a series of pyridyl vicinal dicarbanion bonded $Ag_{13}$ nanoclusters with an open-shell electronic structure are synthesized and characterized for the first time. The newly developed two-step synthetic method involves the occurrence of an inter-cluster oxidative coupling reaction and the assembly of diide-centered $Ag_4$ clusters with *in situ* generated low-valence metal atoms to generate organosilver nanoclusters. Moreover, the aryl dicarbanion ligands on the nanocluster surface further undergo an intra-cluster oxidative coupling to produce homo-coupling products and larger nanocluster species, providing a new perspective for the dynamic evolution of organometallic species in metal catalysis, from isolated metal atoms through low nuclearity organometallic clusters to nanoclusters and nanoparticles. As the *in situ* generated organometallic nanoclusters have been deemed to be active species in many metal-catalyzed reactions, we believe that this study not only reveals novel inter- and intra-cluster coupling steps in different stages, but also is reminiscent of the evolution of cluster species in metal-catalyzed reactions.

## Experimental

### Materials and methods

All commercially available chemicals were used without further purification. The solvents used in this study were processed by standard procedures. $^1$H-NMR and COSY experiments were carried out on a JEOL ECX-400 MHz instrument. Mass spectra were obtained using a Thermo Scientific Exactive Orbitrap instrument and TIMS-TOF mass spectrometer (Bruker Daltonics, Bremen, Germany). DOSY experiments were carried out on a Bruker Avance 600 MHz instrument using a 5 mm TXI H–C/N–D Z-GRD probe. 2D sequence for diffusion measurements were conducted using stimulated echo with 1 spoil gradient. UV-vis spectra were recorded on a Cary 7000 UV-vis-NIR spectrophotometer. EPR experiments were carried out using a JEOL JES-FA200 ESR spectrometer. Transmission electron microscopy (TEM) measurements were performed on a Hitachi H-7650 microscope. The XPS measurement was carried out in a Kratos ULTRA AXIS DLD ultrahigh vacuum photoelectron spectroscopy system. A monochromatic Al Kα X-ray (1486.6 eV) excitation source was used as an excitation source. The details of X-ray crystallographic measurements are summarized in the ESI.† Octamethylazacalix[8]pyridine (**Py[8]**) was synthesized according to the reported synthetic protocol by Pd-catalyzed fragment coupling reactions between a terminal dibrominated linear pentamer and a terminal diaminated linear trimer.[24] Detailed synthesis procedures for aryl dicarbanion bonded $Ag_4$ clusters and hexakis-aryl dicarbanion bonded $Ag_{13}$ nanoclusters are summarized below.

### Synthesis of aryl dicarbanion bonded $Ag_4$ clusters

**Complex $^{Me}$PyAg$_5$ ([Ag$_5$(C$_6$NH$_5$)(Py[8])](CF$_3$SO$_3$)$_3$).** In a 10 mL round-bottom flask, $AgCF_3SO_3$ (51.2 mg, 0.2 mmol) and **Py[8]**

© 2022 The Author(s). Published by the Royal Society of Chemistry

Open Access Article. Published on 14 June 2022. Downloaded on 1/1/2026 2:59:02 AM. This article is licensed under a Creative Commons Attribution-NonCommercial 3.0 Unported Licence.

(17.0 mg, 0.02 mmol) were dissolved in 1.5 mL $CH_2Cl_2$/$CH_3OH$ (v/v 1 : 1) solution at room temperature. After stirring for five minutes, the propargylamine dissolved in 0.5 mL $CH_2Cl_2$/$CH_3OH$ (v/v 1 : 1) solution was added dropwise. Then acetone (23.2 mg, 0.4 mmol) was added to the system. After stirring for 10 hours under lucifugal conditions, a black precipitate was produced. After centrifugation, the supernatant was processed under vacuum to produce a yellow crude oily product. Yellow block crystals of complex $^{Me}$**PyAg$_5$** were isolated by diffusion of diethyl ether into a concentrated $CH_2Cl_2$/$CH_3OH$ (v/v 1 : 1) solution of crude product. Yield: 61% (23.2 mg). $^1$H NMR (400 MHz, acetone-$d_6$): $\delta$ 8.51–8.23 (m, 2H), 8.08 (m, 4H), 7.67 (s, 2H), 7.61–7.37 (m, 10H), 6.91 (d, $J$ = 7.3 Hz, 1H), 6.85 (d, $J$ = 7.7 Hz, 3H), 6.15 (d, $J$ = 8.2 Hz, 1H), 6.09 (d, $J$ = 8.0 Hz, 3H), 3.87 (s, 12H), 3.14 (s, 12H), 2.42 (s, 3H). HR-MS (ESI) calcd for $C_{56}H_{53}Ag_5F_6N_{17}O_6S$ ([$^{Me}$**PyAg$_5$**–OTf$^-$]$^+$) 1777.8949, found 1777.9000. The crystal structure of the complex $^{Me}$**PyAg$_5$** is shown in Fig. 1.

**Complex $^{n\text{-}Pr}$PyAg$_5$ ([Ag$_5$(C$_8$NH$_9$)(Py[8])](CF$_3$SO$_3$)$_3$).** The synthetic procedure of complex $^{n\text{-}Pr}$**PyAg$_5$** is similar to that of $^{Me}$**PyAg$_5$**, but with 2-pentanone (34.3 mg, 0.4 mmol) in place of acetone. The crystallization yield of $^{n\text{-}Pr}$**PyAg$_5$** as yellow block crystals is 56% (21.8 mg). $^1$H NMR (400 MHz, acetone-$d_6$) $\delta$ 8.42–8.23 (m, 3H), 8.09–7.95 (m, 6H), 7.81 (s, 1H), 7.77–7.67 (m, 3H), 7.57–7.41 (m, 8H), 7.11 (t, $J$ = 8.1 Hz, 2H), 6.83 (d, $J$ = 7.8 Hz, 5H), 6.08 (d, $J$ = 7.3 Hz, 2H), 5.82 (d, $J$ = 7.8 Hz, 2H), 3.88 (s, 12H), 3.13 (d, $J$ = 17.0 Hz, 12H). HR-MS (ESI) calcd for $C_{58}H_{57}Ag_5F_6N_{17}O_6S_2$ ([$^{n\text{-}Pr}$**PyAg$_5$**–OTf$^-$]$^+$) 1805.9262, found 1805.9270. The crystal structure of $^{n\text{-}Pr}$**PyAg$_5$** is shown in Fig. S9.†

**Complex $^{Ph}$PyAg$_5$ ([Ag$_5$(C$_{11}$NH$_7$)(Py[8])](CF$_3$SO$_3$)$_3$).** Acetophenone (48.1 mg, 0.4 mmol) is used to replace acetone in the synthetic procedure of $^{Ph}$**PyAg$_5$**. The yield of $^{Ph}$**PyAg$_5$** as yellow block crystals is 23% (9.2 mg). $^1$H NMR (400 MHz, acetone-$d_6$) $\delta$ 8.42–8.23 (m, 3H), 8.09–7.95 (m, 6H), 7.81 (s, 1H), 7.77–7.67 (m, 3H), 7.57–7.41 (m, 8H), 7.11 (t, $J$ = 8.1 Hz, 2H), 6.83 (d, $J$ = 7.8 Hz, 5H), 6.08 (d, $J$ = 7.3 Hz, 2H), 5.82 (d, $J$ = 7.8 Hz, 2H), 3.88 (s, 12H), 3.13 (d, $J$ = 17.0 Hz, 12H). HR-MS (ESI) calcd for $C_{61}H_{55}Ag_5F_6N_{17}O_6S_2$ ([$^{Ph}$**PyAg$_5$**–OTf$^-$]$^+$) 1839.9106, found 1839.9078. The crystal structure of $^{Ph}$**PyAg$_5$** is shown in Fig. S10.†

### Synthesis of hexakis-aryl dicarbanion bonded $Ag_{13}$ nanoclusters

**Complex $^{Me}$PyAg$_{13}$ ([Ag$_{13}$(C$_6$NH$_5$)$_6$H$_6$](SO$_3$CF$_3$)$_6$).** In a 5 mL glass bottle, $^{Me}$**PyAg$_5$** (39.2 mg, 0.02 mmol) was dissolved in 2.0 mL acetone at room temperature. Then trifluoromethanesulfonic acid (HOTf) (17.6 μL, 0.2 mmol) was added to the system and the solution was stirred for 5 hours under lucifugal conditions. After centrifugation, the supernatant was diffused by diethyl ether to give brown bulk crystals. Yield: 52% (4.2 mg). $^1$H NMR (400 MHz, acetone-$d_6$): $\delta$ 8.94 (s, 1H), 8.31–8.19 (m, 10H), 7.98 (s, 1H), 2.59 (s, 15H), 2.48 (s, 3H). HR-MS (ESI) calcd for $C_{42}H_{36}Ag_{13}F_{18}N_6O_{18}S_6$ ([$^{Me}$**PyAg$_{13}$**]$^+$) 2847.7919, found 2847.7750. The crystal structure of $^{Me}$**PyAg$_{13}$** is shown in Fig. 2. The synthetic procedures of other hexakis-aryl dicarbanion bonded $Ag_{13}$ nanoclusters $^{n\text{-}Pr}$**PyAg13** and $^{Ph}$**PyAg$_{13}$** are similar to those for $^{Me}$**PyAg$_{13}$**, using the corresponding aryl dicarbanion bonded $Ag_4$ clusters in place of $^{Me}$**PyAg$_5$**.

**$^{n\text{-}Pr}$PyAg$_{13}$ [Ag$_{13}$(C$_8$NH$_9$)H$_6$](CF$_3$SO$_3$)$_6$.** Yield: 47% (4.1 mg, brown bulk crystals). $^1$H NMR (400 MHz, acetone-$d_6$): $\delta$ 8.95 (s, 1H), 8.26 (m, 10H), 7.98 (s, 1H), 2.83 (t, 12H), 1.79 (m, 12H), 0.99 (m, 18H). HR-MS (ESI) calcd for $C_{54}H_{60}Ag_{13}F_{18}N_6O_{18}S_6$ ([$^{n\text{-}Pr}$**PyAg$_{13}$**]$^+$) 3017.9637, found 3018.0814. The crystal structure of $^{n\text{-}Pr}$**PyAg$_{13}$** is shown in Fig. S28.†

**$^{Ph}$PyAg$_{13}$ [Ag$_{13}$(C$_{11}$NH$_7$)H$_6$](CF$_3$SO$_3$)$_6$.** Yield: 23% (2.1 mg, brown bulk crystals). $^1$H NMR (400 MHz, acetone-$d_6$): $\delta$ 8.77 (s, 6H), 8.53 (s, 6H), 7.90 (s, 12H), 7.66 (s, 18H). HR-MS (ESI) calcd for $C_{72}H_{48}Ag_{13}F_{18}N_6O_{18}S_6$ ([$^{Ph}$**PyAg$_{13}$**]$^+$) 3221.8695, found 3221.8822. The crystal structure of $^{Ph}$**PyAg$_{13}$** is shown in Fig. S30.†

## Data availability

The X-ray crystallographic coordinates for structures reported in this work have been deposited at the Cambridge Crystallographic Data Center (CCDC), under deposition number CCDC-1996369 ($^{Me}$**PyAg$_5$**), CCDC-2062353 ($^{n\text{-}Pr}$**PyAg$_5$**), CCDC-2062351 ($^{Ph}$**PyAg$_5$**), CCDC-1995296 ($^{Me}$**PyAg$_{13}$**), CCDC-2062348 ($^{n\text{-}Pr}$**PyAg$_{13}$**), CCDC-2062349 ($^{Ph}$**PyAg$_{13}$**), CCDC-2175048 (protonated **Py[8]**), CCDC-1995303 (protonated 2,2′-dimethyl-4,4′-bipyridine), CCDC-2060712 (protonated 2,2′-dipropyl-4,4′-bipyridine). These data can be obtained free of charge from the Cambridge Crystallographic Data Centre *via* **www.ccdc.cam.ac.uk/data_request/cif**. For full characterization data including UV-vis spectra, High-resolution ESI-MS, EPR, NMR, XPS, IR, TEM, DFT calculations and experimental details, see the ESI.† Any further relevant data are available from the authors upon reasonable request.

## Author contributions

L. Z. conceived and supervised the project. The synthetic experiments and structural characterizations were carried out by C.-C. L. EPR measurements were performed by S. Z. R. J. and Y. X. provided assistance in ESI-MS measurements. C.-C. L., S. Z., J. T. and L. Z. co-wrote the manuscript. All authors discussed the results and commented on the manuscript.

## Conflicts of interest

There are no conflicts to declare.

## Acknowledgements

Financial support by the National Natural Science Foundation of China (22025105, 21821001, 91956125 and 22074075) is gratefully acknowledged.

## References

1 (*a*) D. B. Eremin and V. P. Ananikov, *Coord. Chem. Rev.*, 2017, **346**, 2; (*b*) A. M. Trzeciak and A. W. Augustyniak, *Coord. Chem. Rev.*, 2019, **384**, 1; (*c*) L. Liu and A. Corma, *Trends*


© 2022 The Author(s). Published by the Royal Society of Chemistry

Open Access Article. Published on 14 June 2022. Downloaded on 1/1/2026 2:59:02 AM. This article is licensed under a Creative Commons Attribution-NonCommercial 3.0 Unported Licence.

*Chem.*, 2020, **2**, 383; (*d*) J. Oliver-Meseguer, J. R. Cabrero-Antonino, I. Dominguez, A. Leyva-Perez and A. Corma, *Science*, 2012, **338**, 1452; (*e*) M. Kolter and K. Koszinowski, *Chem.–Eur. J.*, 2019, **25**, 13376; (*f*) J. Oliver-Messeguer, L. Liu, S. García-García, C. Canós-Giménez, I. Domínguez, R. Gavara, A. Doménech-Carbó, P. Concepción, A. Leyva-Pérez and A. Corma, *J. Am. Chem. Soc.*, 2015, **137**, 3894; (*g*) A. Corma, P. Concepción, M. Boronat, M. J. Sabater, J. Navas, M. J. Yacaman, E. Larios, A. Posadas, M. A. López-Quintela, D. Buceta, E. Mendoza, G. Guilera and A. Mayoral, *Nat. Chem.*, 2013, **5**, 775; (*h*) M. S. Szulmanowicz, A. Gniewek, W. Gil and A. M. Trzeciak, *ChemCatChem*, 2013, **5**, 1152.

2 (*a*) A. V. Astakhov, O. V. Khazipov, A. Y. Chernenko, D. V. Pasyukov, A. S. Kashin, E. G. Gordeev, V. N. Khrustalev, V. M. Chernyshev and V. P. Ananikov, *Organometallics*, 2017, **36**, 1981; (*b*) S. Kim, F. Loose, M. J. Bezdek, X. Wang and P. J. Chirik, *J. Am. Chem. Soc.*, 2019, **141**, 17900; (*c*) Y. Jin, C. Zhang, X.-Y. Dong, S.-Q. Zang and T. C. W. Mak, *Chem. Soc. Rev.*, 2021, **50**, 2297.

3 (*a*) D. Pun, T. Diao and S. S. Stahl, *J. Am. Chem. Soc.*, 2013, **135**, 8213; (*b*) B. L. Tran, J. L. Fulton, J. C. Linehan, J. A. Lercher and R. M. Bullock, *ACS Catal.*, 2018, **8**, 8441; (*c*) B. L. Tran, J. L. Fulton, J. C. Linehan, M. Balasubramanian, J. A. Lercher and R. M. Bullock, *ACS Catal.*, 2019, **9**, 4106; (*d*) A. Leyva-Pérez, J. Oliver-Meseguer, P. Rubio-Marqués and A. Corma, *Angew. Chem., Int. Ed.*, 2013, **52**, 11554; (*e*) S. Yamazoe, K. Koyasu and T. Tsukuda, *Acc. Chem. Res.*, 2014, **47**, 816; (*f*) R. Jin, C. Zeng, M. Zhou and Y. Chen, *Chem. Rev.*, 2016, **116**, 10346; (*g*) J. Yan, B. K. Teo and N. Zheng, *Acc. Chem. Res.*, 2018, **51**, 3084; (*h*) I. Chakraborty and T. Pradeep, *Chem. Rev.*, 2017, **117**, 8208.

4 D. Canseco-Gonzalez, A. Gniewek, M. Szulmanowicz, H. Müller-Bunz, A. M. Trzeciak and M. Albrecht, *Chem.–Eur. J.*, 2012, **18**, 6055.

5 C. Li, S. Song, Y. Li, C. Xu, Q. Luo, Y. Guo and X. Wang, *Nat. Commun.*, 2021, **12**, 3813.

6 (*a*) T. Murahashi, Y. Hashimoto, K. Chiyoda, M. Fujimoto, T. Uemura, R. Inoue, S. Ogoshi and H. Kurosawa, *J. Am. Chem. Soc.*, 2008, **130**, 8586; (*b*) S. Hu, T. Shima and Z. Hou, *Nature*, 2014, **512**, 413; (*c*) M. Teramoto, K. Iwata, H. Yamaura, K. Kurashima, K. Miyazawa, Y. Kurashige, K. Yamamoto and T. Murahashi, *J. Am. Chem. Soc.*, 2018, **140**, 12682.

7 (*a*) H. Someya, H. Yorimitsu and K. Oshima, *Tetrahedron*, 2010, **66**, 5993; (*b*) N. Takashi and H. Tamio, *Chem. Lett.*, 2005, **34**, 1152; (*c*) G. Fang and X. Bi, *Chem. Soc. Rev.*, 2015, **44**, 8124.

8 (*a*) Y. Kikukawa, Y. Kuroda, K. Yamaguchi and N. Mizuno, *Angew. Chem., Int. Ed.*, 2012, **51**, 2434; (*b*) A. K. Clarke, M. J. James, P. O'Brien, R. J. K. Taylor and W. P. Unsworth, *Angew. Chem., Int. Ed.*, 2016, **55**, 13798; (*c*) H. G. Ghalehshahi and R. Madsen, *Chem.–Eur. J.*, 2017, **23**, 11920; (*d*) S. G. Sudrik, J. Sharma, V. B. Chavan, N. K. Chaki, H. R. Sonawane and K. P. Vijayamohanan, *Org. Lett.*, 2006, **8**, 1089.

9 (*a*) G. M. Whitesides, D. E. Bergbreiter and P. E. Kendall, *J. Am. Chem. Soc.*, 1974, **96**, 2806; (*b*) B. K. Tate, A. J. Jordan, J. Bacsa and J. P. Sadighi, *Organometallics*, 2017, **36**, 964.

10 (*a*) D. Fiedler, R. G. Bergman and K. N. Raymond, *Angew. Chem., Int. Ed.*, 2006, **45**, 745; (*b*) T. A. Bender, M. Morimoto, R. G. Bergman, K. N. Raymond and F. D. Toste, *J. Am. Chem. Soc.*, 2019, **141**, 1701; (*c*) D. M. Kaphan, M. D. Levin, R. G. Bergman, K. N. Raymond and F. D. Toste, *Science*, 2015, **350**, 1235; (*d*) M. D. Levin, D. M. Kaphan, C. M. Hong, R. G. Bergman, K. N. Raymond and F. D. Toste, *J. Am. Chem. Soc.*, 2016, **138**, 9682; (*e*) X. He, Y. Xue, C.-C. Li, Y. Wang, H. Jiang and L. Zhao, *Chem. Sci.*, 2018, **9**, 1481.

11 (*a*) J. Preindl, K. Jouvin, D. Laurich, G. Seidel and A. Fürstner, *Chem.–Eur. J.*, 2016, **22**, 237; (*b*) L. Jašíková, M. Anania, S. Hybelbauerová and J. Roithová, *J. Am. Chem. Soc.*, 2015, **137**, 13647; (*c*) D. Weber, M. A. Tarselli and M. R. Gagné, *Angew. Chem., Int. Ed.*, 2009, **48**, 5733.

12 G. Abbiati, A. Arcadi, G. Bianchi, S. Di Giuseppe, F. Marinelli and E. Rossi, *J. Org. Chem.*, 2003, **68**, 6959.

13 E.-X. Zhang, D.-X. Wang, Q.-Y. Zheng and M.-X. Wang, *Org. Lett.*, 2008, **10**, 2565.

14 (*a*) M. F. Ibad, A. Schulz and A. Villinger, *Organometallics*, 2015, **34**, 3893; (*b*) M. Håkansson, H. Eriksson and S. Jagner, *Inorg. Chim. Acta*, 2006, **359**, 2519.

15 C. Janiak, *J. Chem. Soc., Dalton Trans.*, 2000, 3885.

16 (*a*) V. G. Albano, L. Grossi, G. Longoni, M. Monari, S. Mulley and A. Sironi, *J. Am. Chem. Soc.*, 1992, **114**, 5708; (*b*) X. Liu, J. Chen, J. Yuan, Y. Li, J. Li, S. Zhou, C. Yao, L. Liao, S. Zhuang, Y. Zhao, H. Deng, J. Yang and Z. Wu, *Angew. Chem., Int. Ed.*, 2018, **57**, 11273; (*c*) X.-J. Xi, J.-S. Yang, J.-Y. Wang, X.-Y. Dong and S.-Q. Zang, *Nanoscale*, 2018, **10**, 21013.

17 G. Schön, *Acta Chem. Scand.*, 1973, **27**, 2623.

18 V. K. Kaushik, *J. Electron Spectrosc. Relat. Phenom.*, 1991, **56**, 273.

19 (*a*) K. K. Chakrahari, J.-H. Liao, S. Kahlal, Y.-C. Liu, M.-H. Chiang, J.-Y. Saillard and C. W. Liu, *Angew. Chem., Int. Ed.*, 2016, **55**, 14704; (*b*) V. G. Albano, F. Calderoni, M. C. Iapalucci, G. Longoni, M. Monari and P. Zanello, *J. Cluster Sci.*, 1995, **6**, 107.

20 K. B. Wiberg, *Tetrahedron*, 1968, **24**, 1083.

21 Q. Chem and T. Lu, *J. Comput. Chem.*, 2022, **43**, 539.

22 R. F. W. Bader, *Atoms in Molecules: A Quantum Theory*, Oxford University Press, Oxford, UK, 1990.

23 E. Espinosa, I. Alkorta, J. Elguero and E. Molins, *J. Chem. Phys.*, 2002, **117**, 5529.

24 H.-Y. Gong, X.-H. Zhang, D.-X. Wang, H.-W. Ma, Q.-Y. Zheng and M.-X. Wang, *Chem.–Eur. J.*, 2006, **12**, 9262.

© 2022 The Author(s). Published by the Royal Society of Chemistry